Title for citation

SCIENCE CHINA
Information Sciences

• Supplementary File •

Leveraging ±1st-Order Bragg Diffraction Synergy for Bandwidth Enhancement and Frequency Downshift in Acousto-Optic Modulators

Zixuan ZHONG[1,2], Xueqiao YUAN[3], Wei WU[3], Ziqi ZHONG[1,2], Tongtian REN[1,2], Tao LIU[1,2]
Guolu YIN[1,2], Tao ZHU[1,2*]

[1]*State Key Laboratory of Coal Mine Disaster Dynamics and Control, Chongqing University, Chongqing 400044, China*
[2]*Key Laboratory of Optoelectronic Technology and Systems (Ministry of Education), Chongqing University, Chongqing 400044, China*
[3]*The 26th Research Institute of China Electronics Technology Group, Chongqing 400060, China*

Appendix A Principle of the ±1st-order Bragg diffraction synergy AOM architecture

The incident light $\boldsymbol{a}$, collimated by a collimator, enters AOM1 at an incidence angle θ_{i1} satisfying [1]

$$\theta_{i1} = \frac{\lambda f_{AOM1}}{2nv}, \tag{A1}$$

where λ denotes the wavelength of the incident light, f_{AOM1} represents the center frequency shift of AOM1 (f_{AOM2} for AOM2), n is the refractive index of the acousto-optic crystal, and v is the speed of sound of the crystal. The deflection angle θ_{d1} satisfies

$$\theta_{d1}(t) = \frac{\lambda f_{RF1}(t)}{nv}, \tag{A2}$$

where $f_{RF1}(t)$ denotes the time-varying driving frequency of AOM1 and the deflection angle $\theta_{d1}(t)$ is proportional to $f_{RF1}(t)$. The output deflection angle $\theta_{d2}(t)$ of AOM2 satisfies

$$\theta_{d2}(t) = \frac{\lambda f_{RF2}(t)}{nv}. \tag{A3}$$

The constraint relationship of the driving frequencies $f_{RF1}(t)$ and $f_{RF2}(t)$ satisfies

$$f_{RF1}(t) + f_{RF2}(t) = f_{AOM1} + f_{AOM2} = F. \tag{A4}$$

The physical significance of this constraint can be understood through the dynamic matching relationship of the acousto-optic deflection angles. First, the center frequency of the diffraction synergy AOM (DS-AOM) is defined as its output frequency when both constituent AOMs operate at their respective center frequencies, and the direction of the emergent light $\boldsymbol{c}$ in free space under this condition determines the fixed mirror alignment ($\boldsymbol{c}$ is perpendicular to the mirror surface). Second, when the driving frequencies deviate from f_{AOM1} and f_{AOM2}, consider the forward propagation process depicted in Figure A1: At time t_1, assume the driving frequencies and deflection angles for AOM1 and AOM2 are $f_{RF1}(t_1) = f_1$, $\theta_{d1}(t_1) = \theta_1$ and $f_{RF2}(t_1) = f_2$, $\theta_{d2}(t_1) = \theta_2$, respectively. At time t_2, assume the driving frequency of AOM1 increases by Δf while that of AOM2 remains unchanged, then $f_{RF1}(t_2) = f_1 + \Delta f$, $\theta d_1(t_2) = \theta_1 + \Delta\theta$. As evident from Figure A1, this causes the incidence angle on AOM2 to decrease by $\Delta\theta$. However, the deflection angle $\theta d_2(t_2)$ remains θ_2. Consequently, $\boldsymbol{c}$ at t_2 acquires an additional elevation angle of $\Delta\theta$ in free space compared to t_1, thereby deviating from the perpendicularity condition with the mirror. Therefore, at time t_2, $f_{RF2}(t_2)$ should be decreased by Δf to maintain the original angle of $\boldsymbol{c}$ in free space, satisfying Eq. (A4). Failure to adhere to the constraint given by Eq. (A4) will cause $\boldsymbol{c}$ to deviate from its intended return path, which will result in frequency shift chaos during the backward modulation process and prevents effective coupling into the circulator's output port.

* Corresponding author (email: zhutao@cqu.edu.cn)

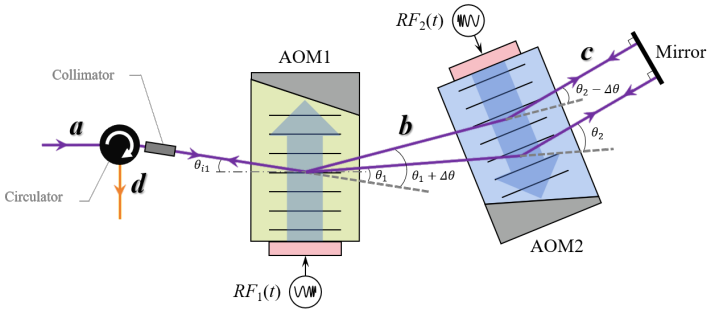

Figure A1 Schematic diagram of the DS-AOM architecture.

Appendix B Principle of the frequency modulation process

Figure B1 shows the principle of the frequency modulation process of the DS-AOM. Continuous light $\boldsymbol{a}$ has a frequency f_a. After undergoing modulation by AOM1, f_a increases. Assuming AOM1 has a tunable bandwidth B_1 centered around f_{AOM1}, corresponding to an RF driving frequency range $f_{RF1} \in [f_{1,min}, f_{1,max}]$, $B_1 = f_{1,max} - f_{1,min}$, the frequency and bandwidth of $\boldsymbol{b}$ satisfy

$$\begin{aligned} f_b &= f_a + f_{RF1}, \\ B_b &= B_1, \end{aligned} \tag{B1}$$

where $f_b \in [f_a + f_{1,min}, f_a + f_{1,max}]$. Subsequently, f_b is decreased upon passing through AOM2. Assuming AOM2 has a tunable bandwidth $B_2 = f_{2,max} - f_{2,min}$, corresponding to the driving frequency range $f_{RF2} \in [f_{2,min}, f_{2,max}]$, the frequency and bandwidth of $\boldsymbol{c}$ output from AOM2 are given by

$$\begin{aligned} f_c &= f_b - f_{RF2}, \\ B_c &= B_1 + B_2, \end{aligned} \tag{B2}$$

where $f_c \in [f_a + f_{1,min} - f_{2,max}, f_a + f_{1,max} - f_{2,min}]$. Subsequently, $\boldsymbol{c}$ is reflected by the mirror and undergoes backward modulation through AOM2 and AOM1. It ultimately exits via the circulator as output light $\boldsymbol{d}$. The frequency and bandwidth of $\boldsymbol{d}$ satisfy the expressions:

$$\begin{aligned} f_d &= f_c - f_{RF2} + f_{RF1}, \\ B_d &= 2(B_1 + B_2), \end{aligned} \tag{B3}$$

where $f_d \in [f_a + 2(f_{1,min} - f_{2,max}), f_a + 2(f_{1,max} - f_{2,min})]$. Consequently, the DS-AOM's tunable bandwidth theoretically equals twice the sum of the individual AOM bandwidths. Furthermore, when the condition $f_{1,min} = f_{2,max}$ is satisfied, the frequency shift of DS-AOM can be continuously tuned starting from zero. Figure B1 illustrates the frequency modulation process under the condition $f_{1,min} = f_{2,max}$, which explains why $\boldsymbol{a}$ to $\boldsymbol{d}$ share the same frequency baseline and enables the DS-AOM to fully achieve frequency band downshift.

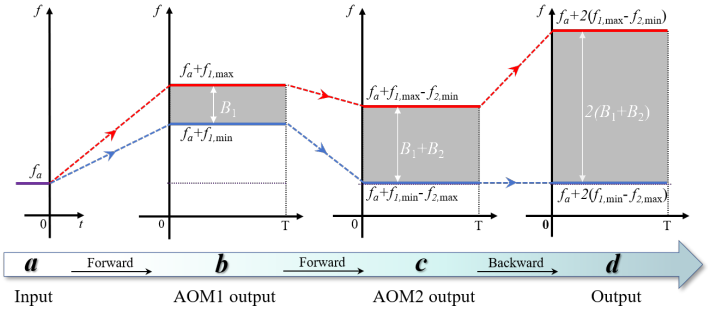

Figure B1 Frequency modulation process of the DS-AOM.

Appendix C Fabrication of the DS-AOM

The optical path configuration and packaging layout of the DS-AOM is shown in Figure C1. The DS-AOM is compactly packaged within a metal housing measuring $80 \times 43 \times 20$ mm^3, featuring single mode fiber input/output ports and RF1/RF2 radio frequency interfaces. The optical components within the module are rigidly fixed using laser welding and hermetic

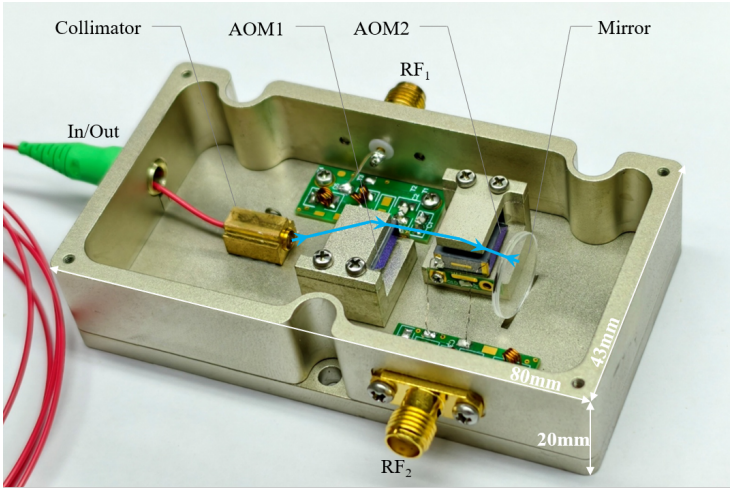

Figure C1 Optical path configuration and packaging layout of the DS-AOM.

packaging, ensuring robust stability against environmental variations. Figure A1 and Figure C1 depict the identical system viewed from opposite sides (front vs. back), maintaining equivalent physical significance.

Tellurium dioxide (TeO_2) is a commonly used acousto-optic crystal due to its high efficiency and broad transmission window. Both AOM1 and AOM2 employ TeO_2 crystals to meet the modulation requirements of the C-band. The acousto-optic Q-value satisfies the expression

$$Q = \frac{2\pi L\lambda}{n\Lambda^2}, \tag{C1}$$

where L is the acousto-optic interaction length, $\lambda = 1550.12$ nm the optical wavelength, $n = 2.3$ the refractive index of the acousto-optic crystal and Λ the acoustic wavelength. The longitudinal acoustic velocity $v = 4400$ m/s. As established by [2], a Q factor exceeding 4π ensures operation in the Bragg diffraction regime with $> 90\%$ first-order diffraction efficiency. However, bandwidth enhancement necessitates reduced interaction length L, which paradoxically lowers Q and degrades diffraction efficiency. Figure C2 illustrates the relationship between Q factor and acoustic frequency at varying interaction lengths L. The intersection points of each curve with the $Q = 4\pi$ threshold determine the minimum acoustic frequency $f_{AOM}^{(L)}$ required to maintain Bragg diffraction efficiency. Critically, $f_{AOM}^{(L)}$ exhibits an inverse dependence on L, increasing as L decreases. This trade-off requires higher acoustic frequencies to maintain efficiency at shorter L. In DS-AOM fabrication, L was shortened to 0.34 cm. Substituting into Eq. C1 yields $f_{AOM}^{(L)} \approx 130$ MHz, thus constraining $f_{2,min} \geqslant 130$ MHz. Consequently, AOM2 was designed with $f_{2,min} = 130$ MHz, $f_{AOM2} = 180$ MHz and bandwidth $B_2 = 100$ MHz, while AOM1 operates at $f_{AOM1} = 280$ MHz with $B_1 = 100$ MHz. The corresponding drive frequency ranges are $f_{RF1} \in [230, 330]$ MHz and $f_{RF2} \in [130, 230]$ MHz. Theoretically, when $f_{1,min} = f_{2,max} = 230$ MHz, the DS-AOM achieves continuous frequency modulation starting from DC (0Hz).

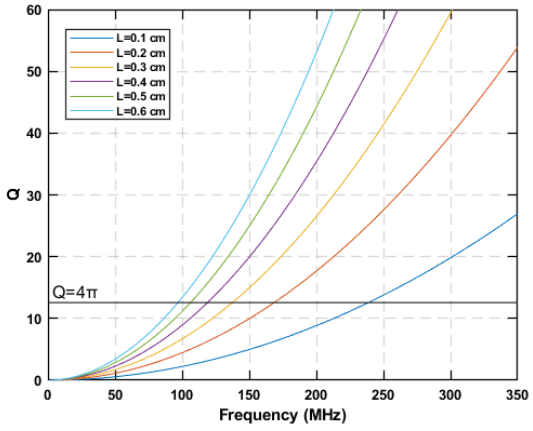

Figure C2 Q Factor vs. Frequency at varying acousto-Optic interaction lengths.

Appendix D Experimental results and discussions

The coherent detection experimental setup for DS-AOM is shown in Figure D1. Continuous-wave light at 1550.12 nm (linewidth $\leqslant$ 100 Hz) from a narrow-linewidth laser (NKT Photonics, E15) is split by a beam splitter with configured power ratios of 90% and 10%. The 90% portion is modulated by the DS-AOM. Moreover, we employ linearly polarized light input, with its polarization direction optimized to be perpendicular to the acousto-optic interaction plane (o-polarized), to ensure polarization stability during the diffraction process. Two RF signals ($RF_1(t)$ and $RF_2(t)$) generated by an AWG (Spectrum, M4i.6631) are amplified through separate driver amplifiers before being fed into their respective AOMs. Their frequencies (f_{RF1} and f_{RF2}) are centered at 280 MHz and 180 MHz, respectively, with $f_{RF1} \in [230, 330]$MHz and $f_{RF2} \in [130, 230]$MHz. The 10% reference beam and the circulator output are combined in a 2×2 coupler to generate a beat signal, which is detected by a BPD (Thorlabs PDB-430C, 1.6 GHz). Then, the DAQ (Spectrum, M4i.2221) digitizes the photocurrent for host computer processing.

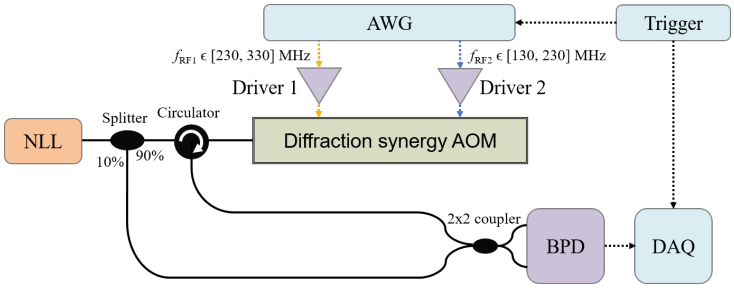

Figure D1 Experimental setup. NLL: narrow linewidth laser, AWG: arbitrary waveform generator, BPD: balanced photodetector, DAQ: data acquisition card.

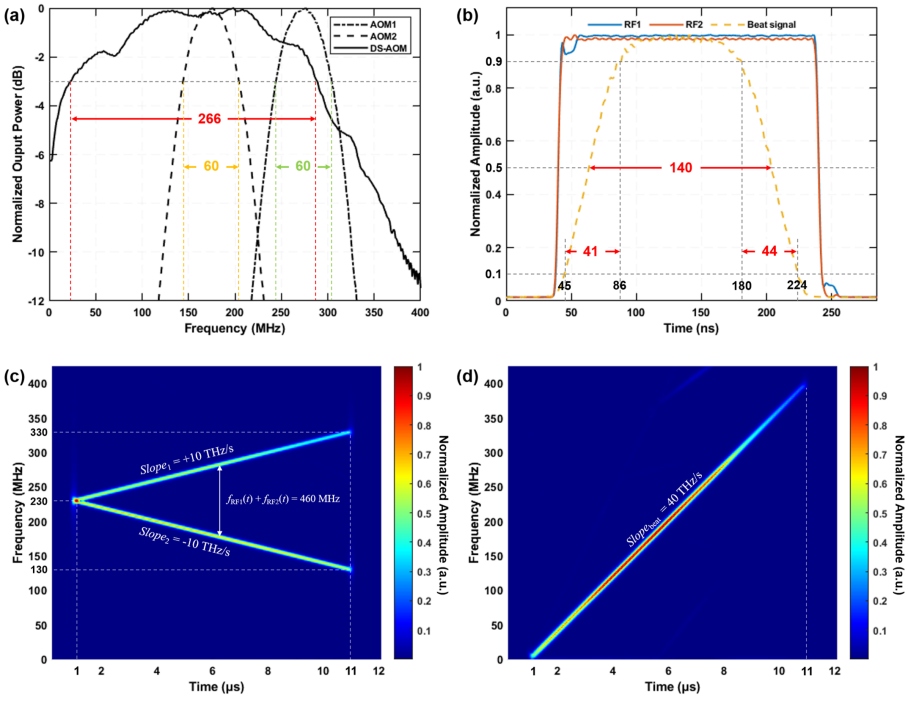

Figure D2 Experimental results of the DS-AOM. (a) Bandwidth performance. (b) Transient time-domain response. (c) Time-frequency characteristics of the drive signals. (d) Time-frequency characteristics of the beat signal.

Figure D2(a) presents the measured bandwidth results of the AOMs. To characterize the DS-AOM bandwidth, the NLL source power was set to 5 mW. The AWG outputed stepped-frequency pulsed signals with f_{RF1} swept from 230.25 MHz to 330 MHz in 0.25 MHz increments. Pulse duration and interval were maintained at 20 μs and 0.2 μs, respectively, while f_{RF2} satisfied the frequency constraint specified in Eq. (A4). According to Eq. (B3), the beat signal comprises 400 frequency components spaced at 1 MHz intervals over the 1–400 MHz range. The normalized output power of these components, obtained via FFT, are indicated by the solid curve in Figure D2(a). For comparison, the device under test was replaced with conventional collimation-focusing AOMs (AOM1 and AOM2). Here, f_{RF1} was stepped in 1 MHz increments from 100 MHz to 350 MHz while maintaining the original pulse interval and duration. The normalized output power results for

these conventional configurations are plotted as dashed lines in Figure D2(a). Evidently, the DS-AOM achieves an output frequency band covering the 1-400 MHz range, consistent with theoretical calculations. The measured 3-dB bandwidth of the DS-AOM is 266 MHz, whereas the conventional AOMs exhibit 3-dB bandwidths of only 60 MHz each. Therefore, compared to the conventional architecture, this work achieves a 4.4-fold enhancement in the 3-dB bandwidth. The output bandwidth of the conventional AOMs is constrained by the coupling angle limitations of the focusing optics; as evidenced by the dashed lines in Figure D2(a), the output power decreases rapidly as the frequency deviates from the center frequency. In contrast, the output power roll-off of the DS-AOM primarily depends on the intrinsic bandwidth performance of the constituent AOMs and the magnitude of the drive voltage, resulting in a more irregular profile.

Compared to conventional AOM architectures, the DS-AOM demonstrates significant advantages in effective bandwidth, with its 3-dB frequency band shifted downward to the [23, 289] MHz range. Although simple multi-stage cascading—for instance, serial connection of conventional +1st-order diffraction AOMs or using mirrors/loops for multiple modulations—can accumulate frequency shifts, the associated power roll-off at the band edges accumulates multiplicatively due to the persistent use of focusing optics for fiber coupling in each stage (as shown by the dashed lines in Figure D2). This leads to significantly lower bandwidth expansion efficiency than the DS-AOM's synergistic mechanism. In the DS-AOM, free-space coupling between AOMs avoids both the angular constraints of fiber coupling and the cumulative band-edge roll-off effect, thereby greatly improving the effective system bandwidth. Although the introduction of the circulator and the 2-pass diffraction process result in slightly reduced extinction ratio and increased insertion loss (40 dB and 6.2 dB, respectively), these performance parameters (including bandwidth) could be further optimized through strategies such as multi-stage cascading optimization and hold potential for future on-chip integration [3, 4]. For example, a DS-AOM module with a bandwidth of [1, 400] MHz can be regarded as a basic unit. When two such units are connected in series, the total bandwidth can theoretically be extended to [2, 800] MHz, while the extinction ratio is enhanced. However, limitations in insertion loss and system complexity mean that its scalability involves a design trade-off among bandwidth, insertion loss, system complexity, and cost. Furthermore, factors such as minor time discrepancies of drive signals and optical path propagation delays may cause a slight reduction in the modulated pulse width (on the order of a few nanoseconds as indicated in Figure D2(b)). When the DS-AOM is used for frequency-sweeping modulation, such delay discrepancies may also lead to a minor offset in the initial frequency shift. In practical implementations, this effect can be either neglected within acceptable tolerance or mitigated through time-domain alignment operations by compensating for the relative delay between the two drive signals.

References

1 Yariv A, Yeh P. Photonics: Optical Electronics in Modern Communications. Oxford University Press, 2007: 446–461
2 Young Jr E H, Yao S K. Design considerations for acousto-optic devices. Proc. IEEE, 1981, 69: 54–64
3 Beller J, Shao L B. Acousto-optic modulators integrated on-chip. Light Sci. Appl., 2022, 11: 240
4 Erdil M, Izhar Y, Deng Y, et al. Wideband, Efficient AlScN-Si Acousto-Optic Modulator Integrated on a Commercially Available Silicon Photonics Process. ACS Photonics, 2025, 12: 2356–2363